Precision Engineering 34 (2010) 218–230

Contents lists available at ScienceDirect

Precision Engineering

journal homepage: www.elsevier.com/locate/precision

Periodic error calculation from spectrum analyzer data

Hyo Soo Kim, Tony L. Schmitz*

Department of Mechanical and Aerospace Engineering, University of Florida, Gainesville, FL 32608, USA

ARTICLE INFO

Article history:
Received 3 September 2008
Received in revised form 27 May 2009
Accepted 3 June 2009
Available online 11 June 2009

Keywords:
Interferometry
Displacement
Periodic error
Nonlinearity
Frequency
Monte Carlo

ABSTRACT

This paper describes the Monte Carlo evaluation of a single equation that can be used to determine periodic error magnitudes from spectrum analyzer data. In this approach, the optical interference signal is recorded during constant velocity target motion using a spectrum analyzer and the magnitudes of the individual periodic error contributors are used to calculate error magnitudes. This study builds on prior work by treating the general case where both first and second order error components exist and arbitrary initial phase values are considered. Significant experimental results are presented which verify the new approach.

1. Introduction

It is well known that displacement measuring interferometry offers high accuracy, range, and resolution for non-contact displacement measurement applications. One fundamental accuracy limitation for the commonly selected heterodyne (or two frequency) Michelson-type interferometer is periodic error. This non-cumulative error is inherent to the typical polarization coding approach, where the two (heterodyne) optical frequencies are carried on coincident/collinear, linearly polarized, mutually orthogonal laser beams and are separated/recombined using polarization dependent optics. It is caused by frequency mixing/leakage between the reference (fixed) and measurement (moving) paths. One approach to observing and correcting/compensating periodic error is "velocity scanning" where the optical interference signal is recorded during constant velocity target motion using a spectrum analyzer. This was first described by Patterson and Beckwith [1] and explored further by Badami and Patterson [2]. In this method, the magnitudes of the individual periodic error contributors are isolated in frequency during constant velocity motion. Using this information, the optical setup can either be adjusted to reduce their magnitudes or feedback control can be applied to compensate for the error [1].

The purpose of this paper is to describe the calculation of periodic error magnitude in the presence of both first and second order error components with arbitrary initial phase values. It builds on the error calculations based on the individual first and second order contributions described in Ref. [2], but treats the general case where both components are present.

2. Background

As noted previously, heterodyne Michelson-type interferometers that rely on polarization coding inherently suffer from imperfect separation of the two light frequencies into the measurement and reference paths. This frequency leakage leads to first and second order periodic errors, which exhibit spatial frequencies of one and two cycles per displacement fringe, respectively. In a perfect system, a single frequency travels to the reference target, while a second, single frequency travels to the measurement target. This ideal case is depicted in Fig. 1(a), where f_1 and f_2 represent the two frequencies and f_d indicates the Doppler frequency shift due to motion of the measurement target. Note that $f_d = FF(v/\lambda)$, where FF is the fold factor (equal to two for the system shown in Fig. 1(a)) and v is the measurement target velocity. In Fig. 1(b), frequency leakage is indicated by the dashed lines (leakage) superimposed on the solid (intended) paths.

The reference path, which ideally contains light of only frequency f_1 (expressed in Hz), propagates two signals due to frequency leakage:

$$E_{11}\cos(\omega_1 t - FF\cdot k_1 x_1 + \phi_{11}) \quad \text{and} \quad E_{21}\cos(\omega_2 t - FF\cdot k_2 x_1 + \phi_{21})$$

where ϕ_{ij} are the initial phases of the signals E_{ij}, x_1 represents motion of the reference target, k_1 and k_2 are equal to $2\pi/\lambda_1$ and $2\pi/\lambda_2$ (the two wavelengths λ_1 and λ_2 correspond to the two

* Corresponding author. Tel.: +1 352 392 8909; fax: +1 352 392 1071.
E-mail address: tschmitz@ufl.edu (T.L. Schmitz).

0141-6359/$ – see front matter © 2009 Elsevier Inc. All rights reserved.
doi:10.1016/j.precisioneng.2009.06.001

heterodyne frequencies), respectively, and $\omega_{1,2} = 2\pi f_{1,2}$ (rad/s). In the E_{ij} notation, the first subscript denotes frequency, while the second indicates the path (1 for reference and 2 for measurement) [3]. Similarly, the measurement path, ideally composed of only f_2 light, also contains two signals:

$$E_{22}\cos(\omega_2 t - FF\cdot k_2 x_2 + \phi_{22}) \quad \text{and} \quad E_{12}\cos(\omega_1 t - FF\cdot k_1 x_2 + \phi_{12})$$

where the parameter definitions are analogous. The photodetector current is obtained by squaring the sum of the four E_{ij} terms (the two intended signals have equal subscripts while the two leakage induced signals have unequal subscripts); see Eq. (1):

$$\begin{aligned}
I \propto E^2 &= (E_{11}\cos(\omega_1 t - FF\cdot k_1 x_1 + \phi_{11}) + E_{21}\cos(\omega_2 t - FF\cdot k_2 x_1 + \phi_{21}) \\
&\quad + E_{22}\cos(\omega_2 t - FF\cdot k_2 x_2 + \phi_{22}) + E_{12}\cos(\omega_1 t - FF\cdot k_1 x_2 + \phi_{12}))^2 \\
&= \frac{E_{11}^2}{2}[\cos(2\omega_1 t - 2FF\cdot k_1 x_1 + 2\phi_{11}) + 1] \\
&\quad + \frac{E_{21}^2}{2}[\cos(2\omega_2 t - 2FF\cdot k_2 x_1 + 2\phi_{21}) + 1] \\
&\quad + \frac{E_{22}^2}{2}[\cos(2\omega_2 t - 2FF\cdot k_2 x_2 + 2\phi_{22}) + 1] \\
&\quad + \frac{E_{12}^2}{2}[\cos(2\omega_1 t - 2FF\cdot k_1 x_2 + 2\phi_{12}) + 1] \\
&\quad + E_{22}E_{11}[\cos(\omega_2 t + \omega_1 t - FF\cdot k_2 x_2 - FF\cdot k_1 x_1 + \phi_{22} + \phi_{11}) \\
&\quad + \cos(\Delta\omega t - FF\cdot k_2 x_2 + FF\cdot k_1 x_1 + \phi_{22} - \phi_{11})] \\
&\quad + E_{21}E_{12}[\cos(\omega_2 t + \omega_1 t - FF\cdot k_1 x_2 - FF\cdot k_2 x_1 + \phi_{21} + \phi_{12}) \\
&\quad + \cos(\Delta\omega t + FF\cdot k_1 x_2 - FF\cdot k_2 x_1 + \phi_{21} - \phi_{12})] \\
&\quad + E_{22}E_{12}[\cos(\omega_2 t + \omega_1 t - FF\cdot k_2 x_2 - FF\cdot k_1 x_2 + \phi_{22} + \phi_{12}) \\
&\quad + \cos(\Delta\omega t - FF\cdot k_2 x_2 + FF\cdot k_1 x_2 + \phi_{22} - \phi_{12})] \\
&\quad + E_{21}E_{11}[\cos(\omega_2 t + \omega_1 t - FF\cdot k_2 x_1 - FF\cdot k_1 x_1 + \phi_{21} + \phi_{11}) \\
&\quad + \cos(\Delta\omega t - FF\cdot k_2 x_1 + FF\cdot k_1 x_1 + \phi_{21} - \phi_{11})] \\
&\quad + E_{11}E_{12}[\cos(2\omega_1 t - FF\cdot k_1 x_2 - FF\cdot k_1 x_1 + \phi_{11} + \phi_{12}) \\
&\quad + \cos(FF\cdot k_1 x_2 - FF\cdot k_1 x_1 + \phi_{11} - \phi_{12})] \\
&\quad + E_{21}E_{22}[\cos(2\omega_2 t - FF\cdot k_2 x_2 - FF\cdot k_2 x_1 + \phi_{21} + \phi_{22}) \\
&\quad + \cos(FF\cdot k_2 x_2 - FF\cdot k_2 x_1 + \phi_{21} - \phi_{22})] \qquad (1)
\end{aligned}$$

Three simplifications may be applied to Eq. (1). First, the reference path can be considered as fixed so that x_1 is ideally constant and may be set equal to zero. Second, for a relatively small split frequency between the two heterodyne signals, $\Delta\omega = \omega_2 - \omega_1$ (on the order of MHz for commercial systems), the propagation constants, k_1 and k_2, are nearly equal and a single value, k, may be substituted for each. Third, due to detector bandwidth limitations, terms that oscillate at twice the optical frequency (i.e., $2\omega_1 t$, $2\omega_2 t$, or $\omega_1 t + \omega_2 t$) may be neglected; see Eq. (2):

$$\begin{aligned}
I \propto E^2 &= \left(\frac{E_{11}^2}{2} + \frac{E_{21}^2}{2} + \frac{E_{22}^2}{2} + \frac{E_{12}^2}{2}\right) \quad \textit{Optical Power} \\
&+ E_{22}E_{11}\cos(\Delta\omega t - FF\cdot kx_2 + \phi_{22} - \phi_{11}) \quad \textit{AC Interference (intended)} \\
&+ E_{22}E_{11}\cos(\Delta\omega t - FF\cdot kx_2 + \phi_{22} - \phi_{11}) \\
&\textit{AC Interference (leakage included)} \\
&+ E_{21}E_{12}\cos(\Delta\omega t + FF\cdot kx_2 + \phi_{21} - \phi_{12}) \\
&\textit{AC Reference (due to reference path)} \\
&+ E_{22}E_{12}\cos(\Delta\omega t + \phi_{22} - \phi_{12}) \\
&\textit{AC Reference (due to measurement path)} \\
&+ E_{11}E_{12}\cos(FF\cdot kx_2 + \phi_{11} - \phi_{12}) \quad \textit{DC Interference (frequency 1)} \\
&+ E_{21}E_{22}\cos(FF\cdot kx_2 + \phi_{21} - \phi_{12}) \quad \textit{DC Interference (frequency 2)} \qquad (2)
\end{aligned}$$

Eq. (2) lists all 10 interference terms in a fully leaking two frequency interferometer. The intended *AC Interference* term is defined by the interference of E_{22} and E_{11}. It represents the signal of choice in heterodyne systems. Under constant velocity target motion, this term appears at a frequency[1] of $\Delta f - f_d$ in the spectrum analyzer display. A second *AC Interference* term is obtained due to interference between the leakage terms E_{21} and E_{12}. This term represents second order periodic error and includes a Doppler phase shift ($FF\cdot kx_2$) of equal magnitude but opposite sign relative to the intended *AC Interference* term. Therefore, at constant velocity this term is seen at a frequency of $\Delta f + f_d$. The *AC Reference* terms represent first order periodic error and occur due to interference between the intended

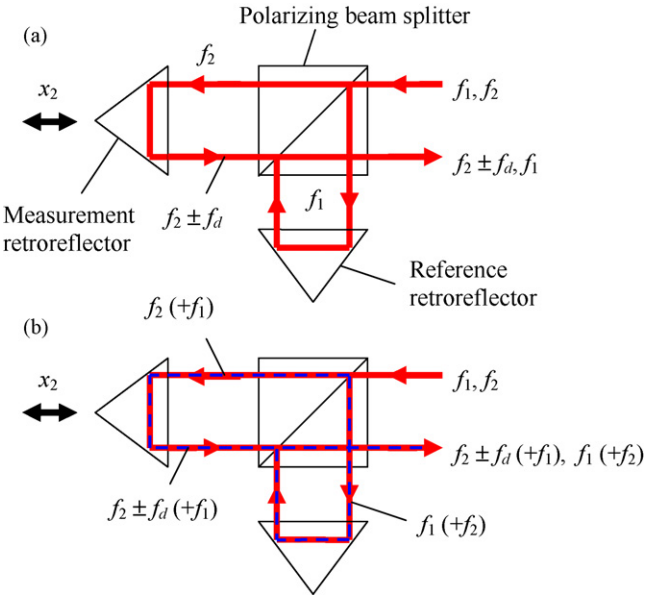

Fig. 1. Schematics for (a) ideal heterodyne interferometer behavior and (b) frequency leakage. The two frequencies, f_1 and f_2, are ideally linearly polarized and orthogonal. This enables the polarizing beam splitter to separate them based on their polarization states.

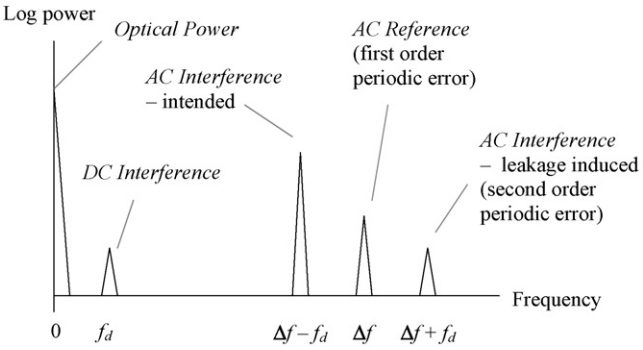

Fig. 2. Frequency spectrum for constant velocity motion in fully leaking heterodyne interferometer. The split frequency, Δf, is $f_2 - f_1$.

[1] The intended *AC Interference* signal may also be upshifted depending on the target motion direction. In this case, the leakage induced *AC Interference* will be downshifted.

and leakage terms of different frequencies that exist in either the reference or measurement paths. They appear at the split frequency Δf; see Fig. 2.

Two *DC Interference* terms also exist because f_1 and f_2 appear in both the measurement and reference paths. For a single frequency, or homodyne, system, the corresponding *DC Interference* term is the selected measurement signal ($E_{21}E_{22}$ for frequency f_2). Because these terms do not include the $\Delta\omega t$ phase offset, they do not appear near the intended *AC Interference* term in the frequency domain and will be neglected in this analysis. The situation is the same for the *Optical Power* terms which contribute a zero frequency offset to the photodetector current regardless of optical path changes.

3. Error calculation

Phasor diagrams present a revealing graphical approach to analyzing periodic error. As described in the previous section, the photodetector current contains not only the desired *AC Interference* term, but also the leakage induced *AC Interference* term and two *AC Reference* terms; see Eq. (2). Because the frequency offset is the same (or nearly so) for the two *AC Reference* terms, they cannot generally be individually distinguished in the spectrum analyzer display. Therefore, we will consider them as a single term with identical frequency and phase in our analysis. These three terms (intended and leakage induced *AC Interference* and *AC Reference* signals), depicted in Fig. 2 spectrum, may be described using three separate phasors in the complex plane.

First, consider the intended *AC Interference* term. It can be described as the phasor $\vec{\Gamma}_0 = \Gamma_0 e^{i(\Delta\omega t - FF\cdot kx_2 + \phi_{22} - \phi_{11})} = \Gamma_0 e^{i(\phi+\phi_0)}$, where Γ_0 is the magnitude (photodector current units of Amperes), $\phi = \omega t - FF\cdot kx_2$ (rad) is the nominal phase change due to the measurement target motion and $\phi_0 = \phi_{22} = \phi_{11}$ (rad) is the (assumed arbitrary) initial phase. This phasor rotates at Δf in the complex plane with no motion and $\Delta f \pm f_d$ depending on the direction while the measurement target is in motion. Alternately, the exponential notation may be replaced by the rectangular coordinate representation:

$$\vec{\Gamma}_0 = \Gamma_0 e^{i(\phi+\phi_0)} = \Gamma_0 \cos(\phi+\phi_0)\vec{j} + \Gamma_0 \sin(\phi+\phi_0)\vec{k},$$

which specifically identifies the real ($\vec{j}$ axis) and imaginary ($\vec{k}$ axis) components. The measurement target position is ideally determined from the instantaneous phase of $\vec{\Gamma}_0$. Under constant velocity conditions, for example, the instantaneous phase grows linearly with time, as does the target position. Conceptually, the phase measuring electronics frequency shift this term back to zero for no motion, or near zero during target motion, by subtracting the reference (split) frequency. For the remainder of the analysis, we consider this frequency shifted condition so that the $\vec{\Gamma}_0$ phasor is rotating at f_d for constant velocity motion; we will assume a counter-clockwise rotation for the selected target direction. Note that after the frequency translation, $\phi = FF\cdot kx_2$; see Fig. 3(a).

Similarly, the *AC Reference* term can be expressed in rectangular coordinates as:

$$\vec{\Gamma}_1 = \Gamma_1 \cos(\phi_1)\vec{j} + \Gamma_1 \sin(\phi_1)\vec{k}.$$

The orientation of this phasor (see Fig. 3(b)) does not vary with time; its direction is fixed by the (assumed arbitrary) initial phase ϕ_1 which, in general, we assume differs from ϕ_0 (see Eq. (2)).Finally, the leakage induced *AC Interference* term can be expressed in rectangular coordinates as:

$$\vec{\Gamma}_2 = \Gamma_2 \cos(\phi-\phi_2)\vec{j} - \Gamma_2 \sin(\phi-\phi_2)\vec{k}.$$

This phasor (see Fig. 3(c)) rotates in the clockwise direction (for counter-clockwise $\vec{\Gamma}_0$ rotation) due to the opposite sign of the Doppler shift. We assume its arbitrary initial phase ϕ_2 differs, in general, from both ϕ_0 and ϕ_1.

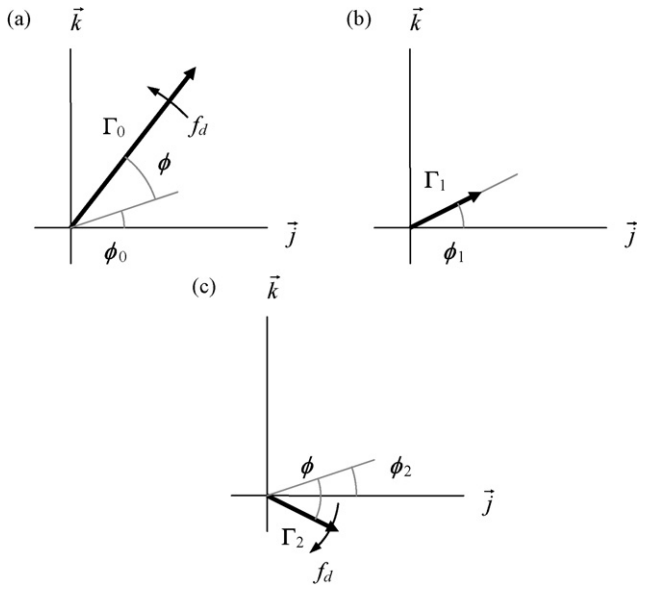

Fig. 3. Phasor diagrams for (a) intended *AC Interference* signal, (b) *AC Reference* signal, and (c) leakage induced *AC Interference* signal.

Prior to determining the periodic error in the general case, let us consider the presence of only $\vec{\Gamma}_0$ and $\vec{\Gamma}_1$, and then only $\vec{\Gamma}_0$ and $\vec{\Gamma}_2$, individually. We select the initial phases to be zero for now to enable direct comparison to Ref. [2]. Fig. 4 depicts the superposi-

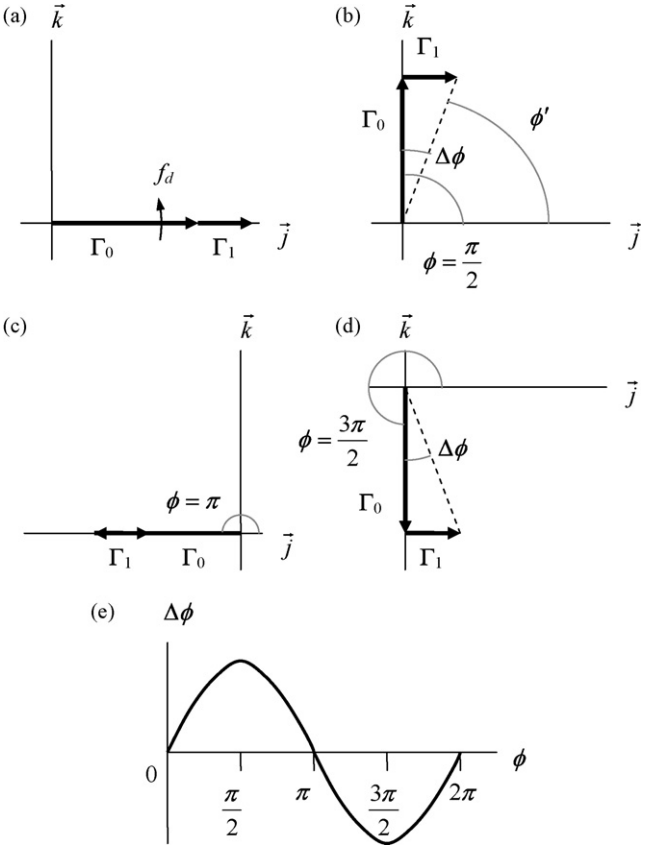

Fig. 4. Periodic error in the presence of $\vec{\Gamma}_0$ and $\vec{\Gamma}_1$ only for various nominal phase angles (rad): (a) 0, (b) $\pi/2$, (c) π, and (d) $3\pi/2$. The single cycle of phase error variation per 2π rad of nominal phase change is shown in (e).

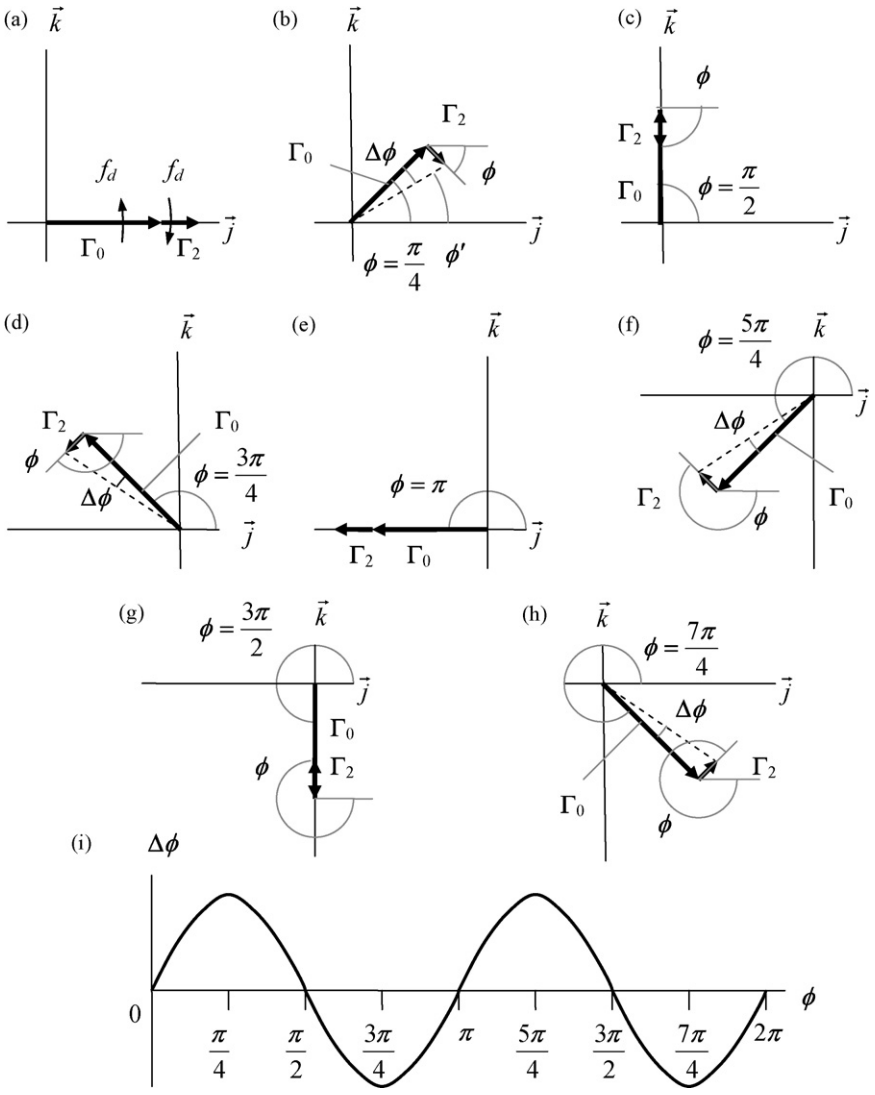

Fig. 5. Periodic error in the presence of $\vec{\Gamma}_0$ and $\vec{\Gamma}_2$ only for various nominal phase angles (rad): (a) 0, (b) $\pi/4$, (c) $\pi/2$, (d) $3\pi/4$, (e) π, (f) $5\pi/4$, (g) $3\pi/2$, and (h) $7\pi/4$. The two cycles of phase error variation per 2π rad of nominal phase change is shown in (i).

tion of the intended *AC Interference* and *AC Reference* phasors ($\vec{\Gamma}_0$ and $\vec{\Gamma}_1$, respectively) at progressing times during constant velocity motion. In Fig. 4(a), an arbitrary time is selected where the nominal phase (from the intended *AC Interference* term) is zero. For zero initial phases, ϕ_0 and ϕ_1, both phasors are directed along the positive real axis. At a later time in Fig. 4(b), the nominal phase is $\phi = \pi/2$ rad, but the actual phase, ϕ', is less than the nominal due to the vector addition of $\vec{\Gamma}_0$ and $\vec{\Gamma}_1$. Recall that the orientation of $\vec{\Gamma}_1$ does not change for the frequency translated condition. The phase error, $\Delta\phi = \phi - \phi'$, is therefore positive and depends on the magnitude of $\vec{\Gamma}_1$. Similar to Fig. 4(a), the phase error in Fig. 4(c) is again zero. In Fig. 4(d), the error is negative, but equal in magnitude to the situation depicted in Fig. 4(b). Fig. 4(e) demonstrates the corresponding single cycle of phase error variation per 2π rad of nominal phase change for first order periodic error. By vector addition, the phase error is: $\Delta\phi = \phi - \phi' = \phi - \tan^{-1}(\Gamma_0 \sin(\phi)/\Gamma_0 \cos(\phi) + \Gamma_1)$ (rad) and the corresponding first order periodic error is:

$$\varepsilon_1 = \frac{1}{FF}\frac{\lambda}{2\pi}\left(\phi - \tan^{-1}\left(\frac{\Gamma_0 \sin(\phi)}{\Gamma_0 \cos(\phi) + \Gamma_1}\right)\right) \text{(nm)} \quad (3)$$

If the maximum first order periodic error, $\varepsilon_{\max,1}$, is assumed to occur when $\phi = \pi/2$ (see Fig. 4(b)), then we can write:

$$\varepsilon_{\max,1} = \frac{1}{FF}\frac{\lambda}{2\pi}\left(\frac{\pi}{2} - \tan^{-1}\left(\frac{\Gamma_0}{\Gamma_1}\right)\right) \text{(nm)}, \quad (3a)$$

which is equivalent to Eq. (5) in Ref. [2] for the small angle approximation. (Eq. (5) in Ref. [2] identifies the maximum phase error magnitude as Γ_1/Γ_0.)

Fig. 5 shows the situation when only $\vec{\Gamma}_0$ (intended *AC Interference* signal) and $\vec{\Gamma}_2$ (leakage induced *AC Interference* signal) are considered. Again selecting zero initial phases, we may pick an arbitrary time when both phasors are directed along the positive real axis; see Fig. 5(a). Because the vectors are counter-rotating, we obtain the geometries shown in Fig. 5(b)–(h) for nominal phase values of $\{\pi/4, \pi/2, 3\pi/4, \pi, 5\pi/4, 3\pi/2, \text{and } 7\pi/4\}$ rad. The characteristic two cycle phase error variation per 2π rad of nominal phase change (second order periodic error) is depicted in Fig. 5(i). The phase error is calculated according to: $\Delta\phi = \phi - \phi' = \phi - \tan^{-1}((\Gamma_0 - \Gamma_2)\sin(\phi)/(\Gamma_0 + \Gamma_2)\cos(\phi))$ (rad) and the corresponding second order periodic error is:

$$\varepsilon_2 = \frac{1}{FF}\frac{\lambda}{2\pi}\left(\phi - \tan^{-1}\left(\frac{(\Gamma_0 - \Gamma_2)\sin(\phi)}{(\Gamma_0 + \Gamma_2)\cos(\phi)}\right)\right) \text{(nm)}. \quad (4)$$

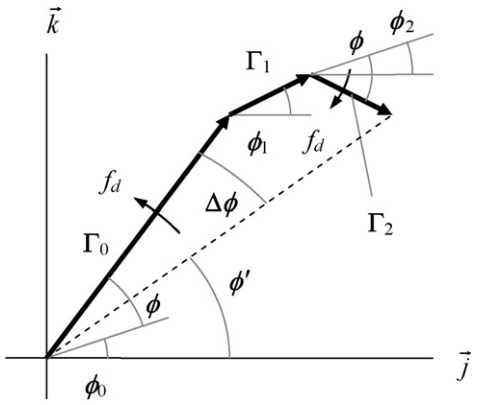

Fig. 6. Phasor diagram for general case where the intended and leakage induced *AC Interference* and *AC Reference* signals are present with arbitrary initial phases.

If the corresponding maximum periodic error is assumed to be obtained when $\phi = \pi/4$ rad (see Fig. 5(b)), so that $\sin(\phi) = \cos(\phi) = \sqrt{2}/2$, then the maximum second order periodic error, $\varepsilon_{\max,2}$, is:

$$\varepsilon_{\max,2} = \frac{1}{FF}\frac{\lambda}{2\pi}\left(\frac{\pi}{4} - \tan^{-1}\left(\frac{\Gamma_0 - \Gamma_2}{\Gamma_0 + \Gamma_2}\right)\right)(\text{nm}), \tag{4a}$$

which agrees with Eq. (6) from Ref. [2] for the small angle approximation. (Eq. (6) from Ref. [2] identifies the maximum phase error magnitude as Γ_2/Γ_0.)

4. Monte Carlo analysis description

In general, however, all three phasors, $\vec{\Gamma}_0$, $\vec{\Gamma}_1$, and $\vec{\Gamma}_2$, are present and the initial phases, ϕ_0, ϕ_1, and ϕ_2, may be assumed to be nonzero, unequal, and uncorrelated. In this case, Eqs. (3) and (4) may not accurately describe the first and second order periodic error magnitudes in the measured phase/position for all combinations of input parameters. To treat the general case, we must first determine an expression for the phase error. Fig. 3(a)–(c) shows the individual phasors with arbitrary phases. They are superimposed in Fig. 6. Based on this geometry, we calculate:

$$\Delta\phi = \phi + \phi_0 - \phi' = \phi + \phi_0 - \tan^{-1} \times \left(\frac{\Gamma_0 \sin(\phi+\phi_0) + \Gamma_1 \sin(\phi_1) - \Gamma_2 \sin(\phi-\phi_2)}{\Gamma_0 \cos(\phi+\phi_0) + \Gamma_1 \cos(\phi_1) + \Gamma_2 \cos(\phi-\phi_2)}\right)(\text{rad}) \tag{5}$$

and the corresponding periodic error is:

$$\varepsilon = \frac{1}{FF}\frac{\lambda}{2\pi}\Delta\phi(\text{nm}) \tag{6}$$

Note that the error is dependent on the nominal phase (of the intended *AC Interference* signal), the three phasor magnitudes, and the initial phases of the three phasors. To evaluate Eq. (6), and identify the periodic error order magnitudes, we apply Monte Carlo simulation. This enables us to incorporate the uniformly distributed, unknown, uncorrelated initial phases. The required steps are:

1. define the values for *FF*, λ, Γ_0, Γ_1, and Γ_2;
2. select random, uniformly distributed values of ϕ_0, ϕ_1, and ϕ_2 from the range $-\pi \le \phi_i \le \pi$, where $i = 0, 1, 2$;
3. compute $\Delta\phi$ from Eq. (5);
4. compute ε from Eq. (6);
5. calculate the discrete Fourier transform of the result from step 4 and normalize the frequency axis to error order (multiply by λ/FF) to identify the individual periodic error contributions from each order; and
6. return to step 2.
7. After many iterations, the periodic error magnitude for each order is selected from the resulting distributions.

As a first comparison between Eqs. (3) and (4) (equivalent to Eqs. (5) and (6) from Ref. [2]) and Eq. (6), we select zero initial phase values. This removes the requirement for Monte Carlo simulation; the periodic error magnitudes are computed directly from the relevant equations, which depend on the phasor magnitudes. Additionally, because spectrum analyzers typically display power data using a logarithmic (dBm) scale, we apply signal amplitudes in this format. To convert from magnitudes, γ_i, in dBm to the (linear) Ampere units for Γ_i included in the previous descriptions, we apply the conversion shown in Eq. (7), where $i = 0, 1, 2$.

$$\Gamma_i = 10^{\gamma_i/20} \tag{7}$$

Fig. 7 displays first and second order error magnitudes for $\gamma_0 = -15$ dBm, $\gamma_1 = -50$ dBm, and values of γ_2 from $\{-50$ to $-20\}$ dBm. In a qualitative sense, the 35 dBm difference between γ_0 and γ_1 corresponds to the attenuation for a well aligned system. While γ_1 and γ_2 do not necessarily vary independently with changes in the optical setup, this approach enables us to provide an initial numerical comparison of the different equations. Experimental results for a conventional setup are provided in a later section. Fig. 7 shows picometer (pm) level agreement between Eq. (6) and Eqs. (3) and (4) for the case where the γ_1 magnitude is negligible. The expected strong variation in second order error with changes in γ_2 is also observed.

In Fig. 8, the attenuation between γ_0 and γ_1 is reduced, $\gamma_0 = -15$ dBm and $\gamma_1 = -30$ dBm. This is characteristic of a misaligned system; note that the first order periodic error is now 10 times larger. The values of γ_2 are varied over the same range. In this case, there is an approximately constant offset in the second order periodic error of 0.8 nm. The residual differences (beyond the second order offset) are at the pm level.

The results for a significantly misaligned system, $\gamma_0 = -15$ dBm and $\gamma_1 = -25$ dBm, are provided in Fig. 9. It is seen that the second order error for Eq. (6) does not increase monotonically with decreased attenuation between γ_0 and γ_2. Rather, a local minimum is seen at $\gamma_2 = -41$ dBm. Fig. 10 is included to show the differences

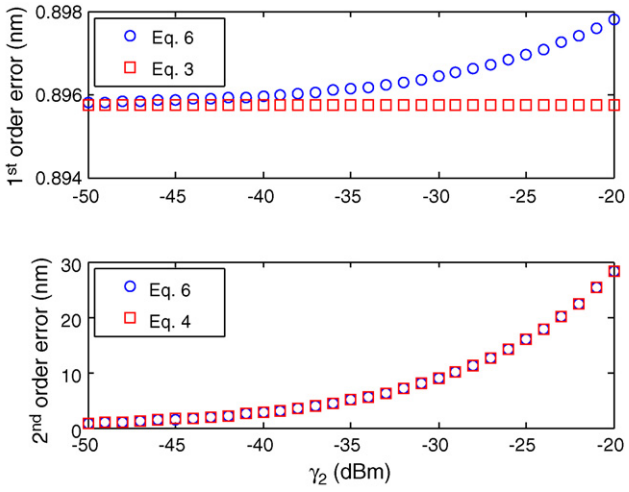

Fig. 7. Comparison between periodic error magnitudes obtained from Eq. (6) and Eqs. (3) and (4) for $\gamma_0 = -15$ dBm, $\gamma_1 = -15$ dBm, and variable γ_2. The agreement is at the picometer level.

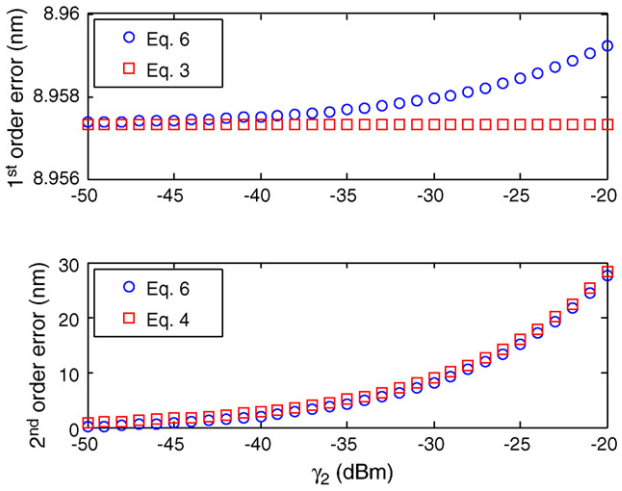

Fig. 8. Comparison between periodic error magnitudes obtained from Eq. (6) and Eqs. (3) and (4) for $\gamma_0 = -15$ dBm, $\gamma_1 = -30$ dBm, and variable γ_2. There is approximately a 0.8 nm offset in the second order periodic error.

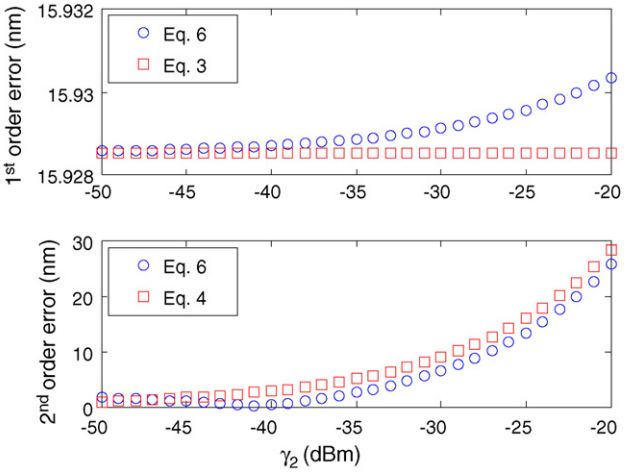

Fig. 9. Comparison between periodic error magnitudes obtained from Eq. (6) and Eqs. (3) and (4) for $\gamma_0 = -15$ dBm, $\gamma_1 = -25$ dBm, and variable γ_2. The second order error no longer increases monotonically for Eq. (6) calculations.

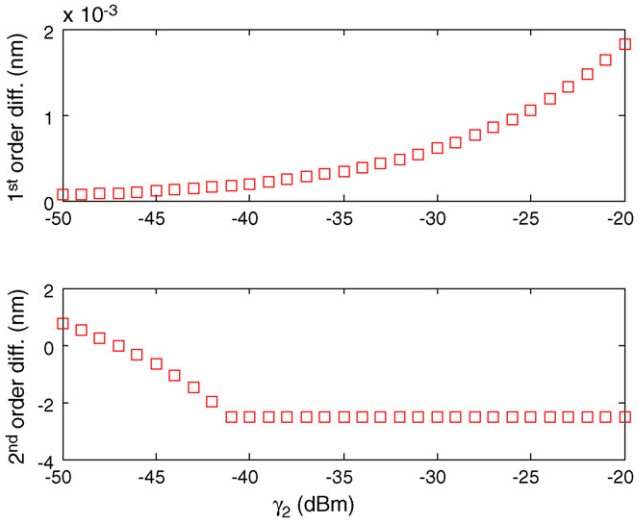

Fig. 10. Difference between periodic error magnitudes obtained from Eq. (6) and Eqs. (3) and (4) for $\gamma_0 = -15$ dBm, $\gamma_1 = 25$ dBm, and variable γ_2.

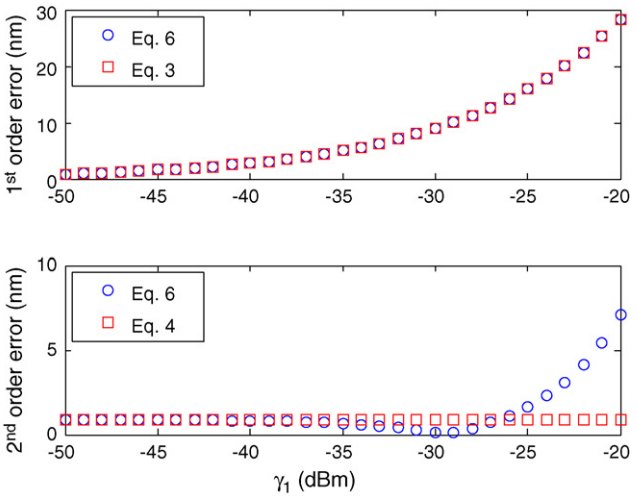

Fig. 11. Comparison between periodic error magnitudes obtained from Eq. (6) and Eqs. (3) and (4) for $\gamma_0 = -15$ dBm, $\gamma_2 = -50$ dBm, and variable.

between Eq. (6) and Eqs. (3) and (4) (Eqs. (3) and (4) results are subtracted from Eq. (6) results).

Next, the γ_0 and γ_2 magnitudes are fixed, and γ_1 is changed. Fig. 11 displays the results for $\gamma_0 = -15$ dBm and $\gamma_2 = -50$ dBm (well aligned setup), while γ_1 is again varied from $\{-50$ to $-20\}$ dBm. As expected the first order periodic error grows with γ_1; the agreement between Eq. (3) and (6) is at the pm level. For Eq. (6), however, the second order error is strongly influenced by the presence of significant γ_1 spectral content. The difference between Eq. (4) and (6) results exceeds 6 nm for the largest misalignment ($\gamma_1 = -20$ dBm). Also, the second order error behavior is again non-monotonic and reaches a local minimum at $\gamma_1 = -30$ dBm when Eq. (6) is applied.

Interesting second order error behavior is also observed for $\gamma_0 = -15$ dBm and $\gamma_2 = -35$ dBm (misaligned setup) and the same variation in γ_1. Fig. 12 shows that the second order error for Eq. (6) is again influenced by γ_1. However, the error now decreases with increasing γ_1 magnitude until a local minimum at -22 dBm is reached, when the error begins increasing again.

Before comparing the equations with experimental results, we now demonstrate the effect of arbitrary initial phase on the periodic error calculations. First, we consider a nonzero initial phase of

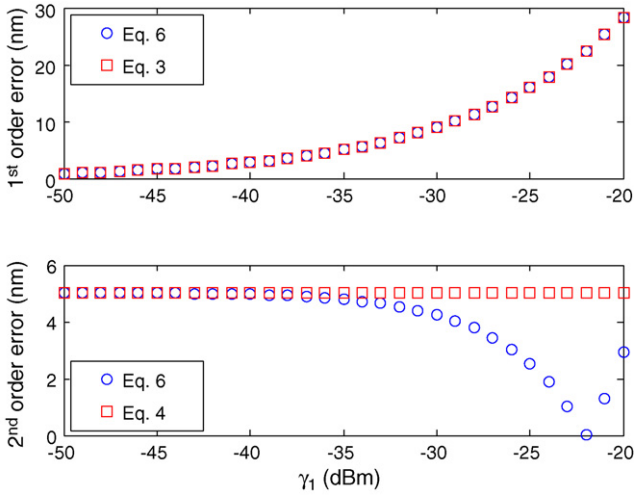

Fig. 12. Comparison between periodic error magnitudes obtained from Eq. (6) and Eqs. (3) and (4) for $\gamma_0 = -15$ dBm, $\gamma_2 = -35$ dBm, and variable γ_1. The second order error from Eq. (6) is again influenced by the variable γ_1 magnitude; it reaches a local minimum at -22 dBm.

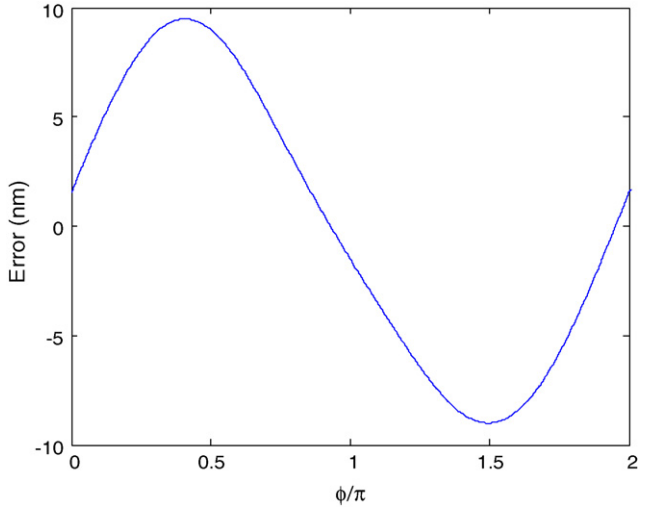

Fig. 13. Periodic error for $\phi_0 = 10^\circ = 0.17$ rad with $\gamma_0 = -15$ dBm, $\gamma_1 = -30$ dBm, $\gamma_2 = -45$ dBm, and $\phi_1 = \phi_2 = 0$.

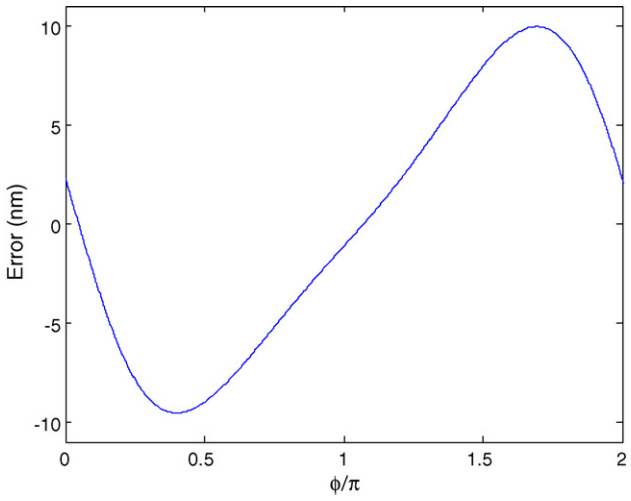

Fig. 15. Periodic error for $\phi_0 = 170^\circ = 2.97$ rad with $\gamma_0 = -15$ dBm, $\gamma_1 = -30$ dBm, $\gamma_2 = -45$ dBm, and $\phi_1 = \phi_2 = 0$.

$\phi_0 = 10^\circ = 0.17$ rad with $\gamma_0 = -15$ dBm, $\gamma_1 = -30$ dBm, $\gamma_2 = -45$ dBm, and $\phi_1 = \phi_2 = 0$. The resulting periodic error over 2π of nominal phase change is shown in Fig. 13. The corresponding discrete Fourier transform magnitude (with frequency normalized to error order) is provided in Fig. 14. The first order periodic error dominates with a magnitude of 8.96 nm. The second order magnitude is 0.82 nm. Small third order content (0.19 nm) is also observed, although this is not typically considered in most analyses. However, if ϕ_0 is changed to $170^\circ = 2.97$ rad, for example, the associated error waveform differs; see Fig. 15. The second order error magnitude now increases to 2.38 nm as shown in Fig. 16. The third order magnitude also increases to 0.38 nm. Using the previously described Monte Carlo simulation, the variation in periodic error magnitudes with ϕ_0 variation between $\pm\pi$ (uniformly distributed) is determined. See Fig. 17, where 1000 iterations were completed. The first order error changes very little, while the second order error varies between 0.80 and 2.39 nm. Analogous results are obtained if the other initial phase values are varied, but are not included here for brevity.

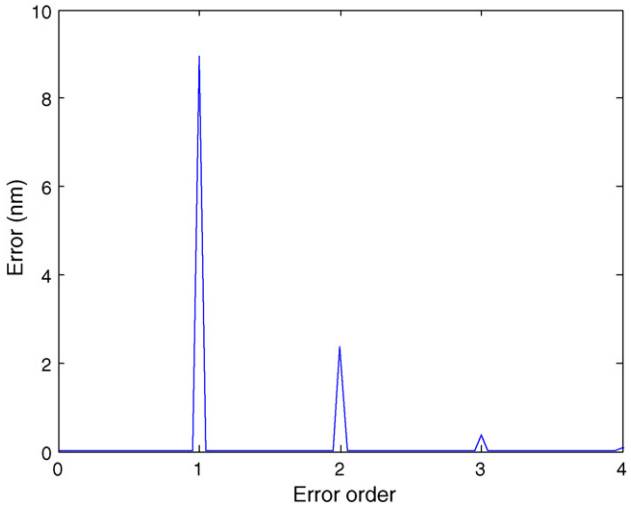

Fig. 16. Periodic error magnitudes for $\phi_0 = 170^\circ = 2.97$ rad with $\gamma_0 = -15$ dBm, $\gamma_1 = -30$ dBm, $\gamma_2 = -45$ dBm, and $\phi_1 = \phi_2 = 0$.

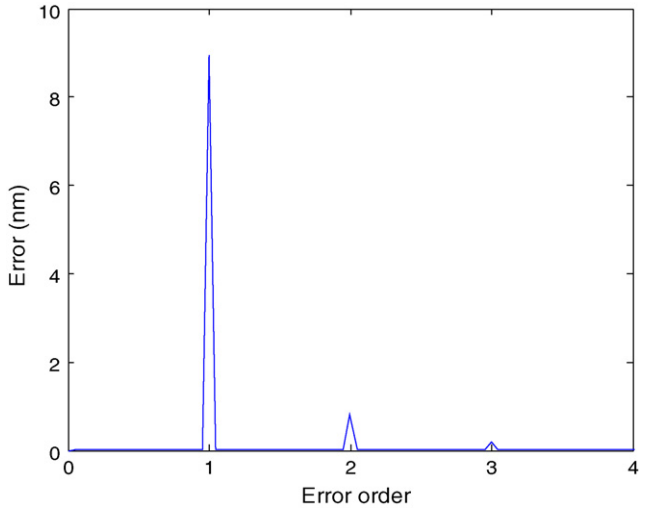

Fig. 14. Periodic error magnitudes for $\phi_0 = 10^\circ = 0.17$ rad with $\gamma_0 = -15$ dBm, $\gamma_1 = -30$ dBm, $\gamma_2 = -45$ dBm, and $\phi_1 = \phi_2 = 0$.

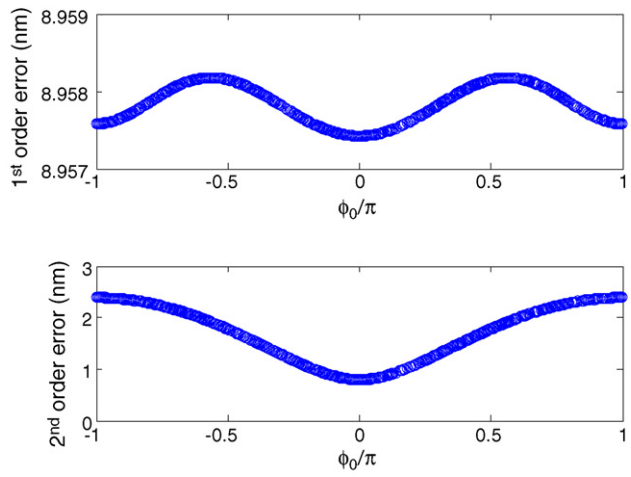

Fig. 17. Variation in periodic error magnitudes for random ϕ_0 values ($\pm\pi$ range) with $\gamma_0 = -15$ dBm, $\gamma_1 = -30$ dBm, $\gamma_2 = -45$ dBm, and $\phi_1 = \phi_2 = 0$.

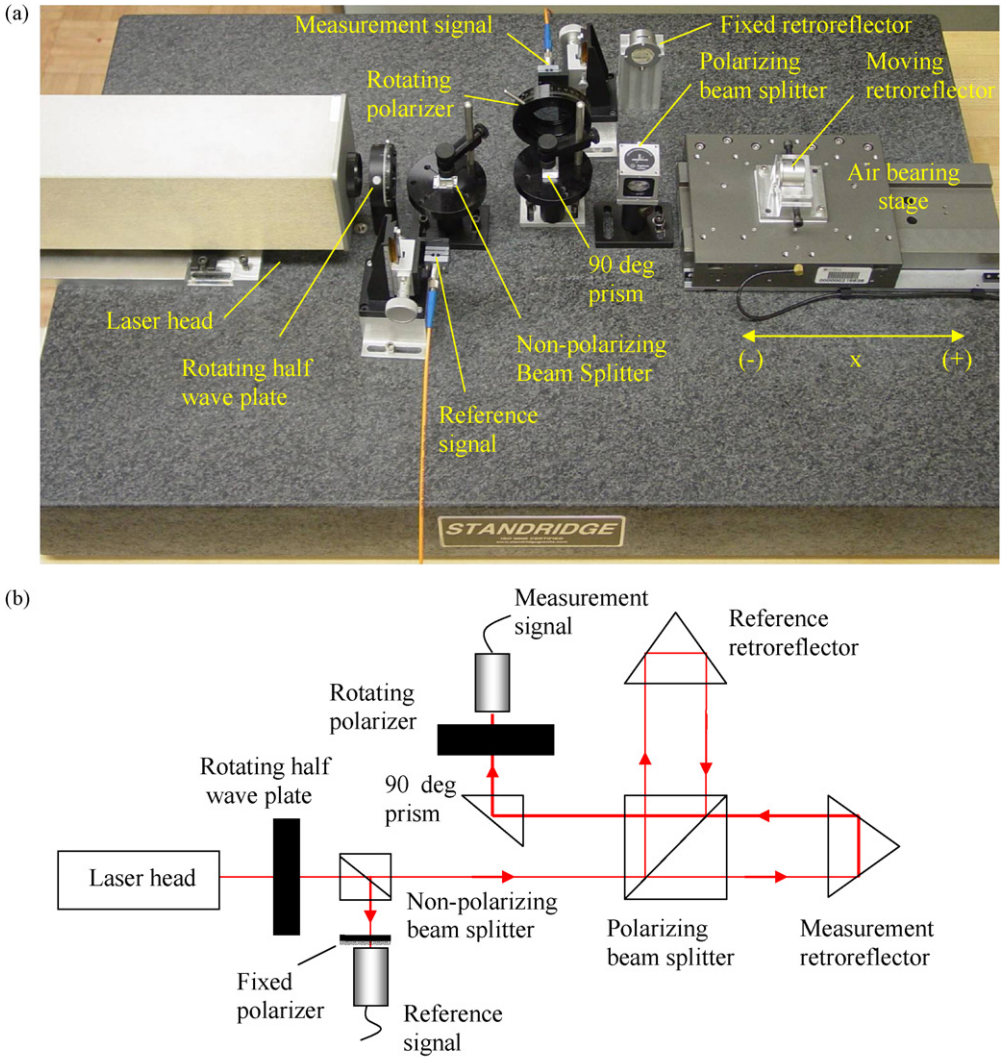

Figure 18: (a) Photograph of single pass, heterodyne interferometer experimental setup. (b) Schematic of setup.

Fig. 18. (a) Photograph of single pass, heterodyne interferometer experimental setup and (b) schematic of setup.

5. Experimental setup description

A photograph and schematic of a traditional heterodyne displacement measuring interferometer setup are provided in Fig. 18. The orthogonal, linearly polarized beams with a frequency difference of approximately 3.65 MHz (Helium–Neon laser source with a Zeeman split) first pass through a half wave plate. Rotation of the half wave plate enables variation in the apparent angular alignment (about the beam axis) between the polarization axes and polarizing beam splitter; deviations in this alignment lead to frequency mixing in the interferometer. The light is then incident on a non-polarizing beam splitter (80% transmission) that directs a portion of the beam to a fiber optic pickup after passing through a fixed angle sheet polarizer (oriented at 45° to the nominal laser orthogonal polarizations). The pickup is mounted on a two rotational degree-of-freedom flexure which enables efficient coupling of the light into the multi-mode fiber optic. This signal is used as the phase reference in the measurement electronics.

The remainder of the light continues to the polarizing beam splitter where it is (ideally) separated into its two frequency components that travel separately to the moving and fixed retroreflectors. Motion of the moving retroreflector is achieved using an air bearing stage. After the beams are recombined in the polarizing beam splitter, they are directed by a 90° prism through a polarizer (or analyzer) with a variable rotation angle. Finally, the light is launched into a fiber optic pickup. This serves as the measurement signal in the measurement electronics (0.3 nm resolution for the single pass configuration).

The intent of this setup was to minimize other well-known error contributors and set various first and second order periodic error magnitudes. To isolate periodic error, the setup was constructed with zero dead path difference (i.e., the distance between the polarization beam splitter and the moving retroreflector was equal to the distance between the polarization beam splitter and the fixed retroreflector at initialization) and small Abbe offset (25 mm). The measurement time (~100 ms) and motion excursions were kept small to minimize the contribution of air refractive index variations due to the environmental changes. Additionally, careful alignment of the air bearing stage axis with the optical axis resulted in small beam shear.

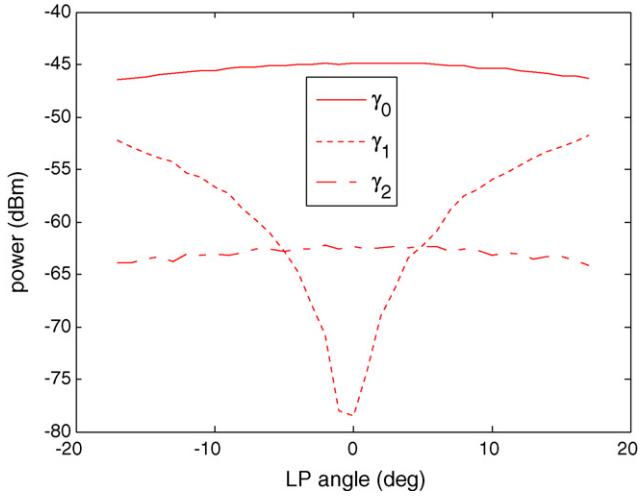

Fig. 19. Variation of γ_0, γ_1, and γ_2 with linear polarizer (LP) angle. The half wave plate (HWP) was fixed at 10° from its nominal orientation (a large misalignment configuration). Strong variation of γ_1 is observed.

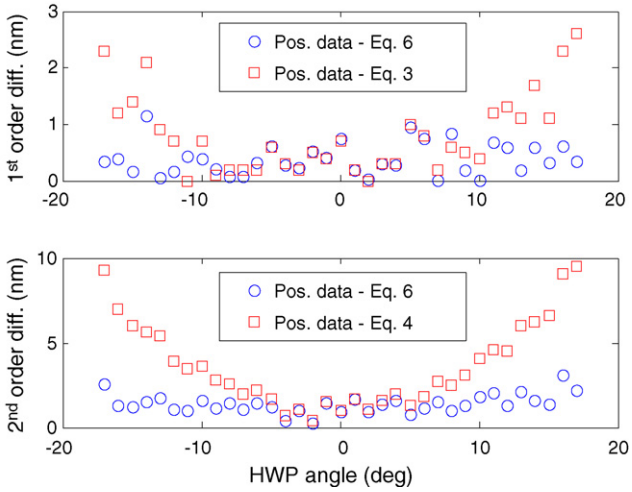

Fig. 21. Differences between magnitudes from Eqs. (3), (4) and (6) and discrete Fourier transform of position data; first order (top) and second order (bottom). The differences were calculated from the errors displayed in Fig. 20.

6. Experimental results

In this section, spectrum analyzer data (γ_0, γ_1, and γ_2 spectral peaks measured in dBm) are used to calculate first and second order periodic error magnitudes via Eqs. (3), (4), and (6). These results are compared with periodic error magnitude values determined from the discrete Fourier transform of position data obtained from traditional phase measuring electronics.

Data were collected for different levels of frequency mixing by varying the linear polarizer and half wave plate angles from their nominal orientations (see Fig. 18). As noted, Eqs. (3), (4), and (6) were applied to compute the corresponding periodic error. Note that Monte Carlo simulation was used to evaluate Eq. (6), which enabled the uniformly distributed, uncorrelated initial phases to be randomly selected over many iterations. In the following analyses, the maximum values from the simulations are presented.

Fig. 19 displays the case where the linear polarizer angle was varied about its nominal orientation (indicated as zero), while the half wave plate angle was fixed at 10° from its nominal angle. A strong variation for γ_1, the *AC Reference* term, is observed while γ_0 and γ_2, the intended *AC Interference* and leakage induced *AC Interference* terms, respectively, are nearly constant. The first order errors calculated by Eqs. (3) and (6) increase with larger misalignment angles and agree with the magnitudes calculated from the position data using the discrete Fourier transform; see the top panel of Fig. 20. However, the second order errors computed using Eqs. (4) and (6) do not agree. As shown in the bottom panel of Fig. 20, Eq. (6) results more closely follow the second order error calculated from the position data.

Fig. 21 shows the difference between Eqs. (3), (4), and (6) calculations and position data (discrete Fourier transform) magnitudes for first and second error order errors; the data from Fig. 20 was analyzed. It is seen that Eqs. (3), (4), and (6) results agree with the position data for small linear polarizer angular misalignments. For large misalignments, however, Eqs. (3) and (4) provide less accurate estimates (2.6 nm difference for first order error and 9.5 nm difference for second order error at the largest misalignment). Eq. (6), on the other hand, agrees to within 1.2 nm for first and 3.0 nm for second order error. These results show that Eq. (6), which considers all three spectral peaks, provides a more accurate estimate

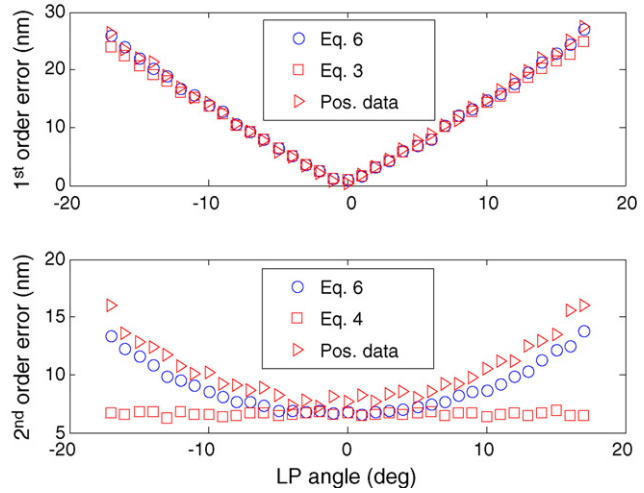

Fig. 20. The magnitudes of first (top) and second (bottom) order periodic errors calculated by Eqs. (3), (4), and (6) are compared to magnitudes computed using the discrete Fourier transform of position data. The agreement is good for first order error, but only Eq. (6) reproduces the second order error.

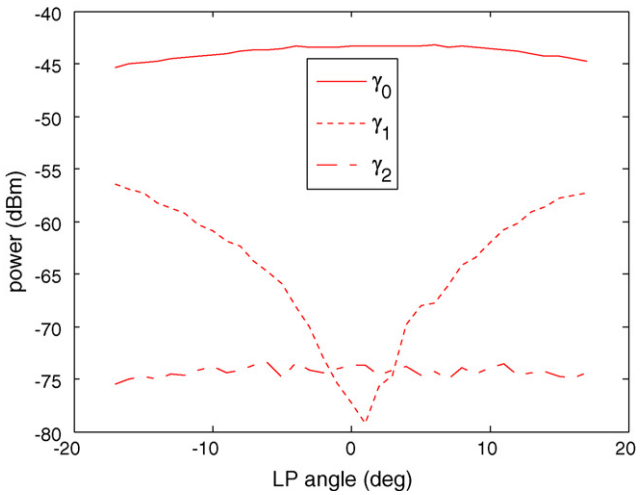

Fig. 22. Variation of γ_0, γ_1, and γ_2 with linear polarizer (LP) angle. The half wave plate was fixed at 5° from its nominal orientation (a medium misalignment configuration). Strong variation of γ_1 is again observed.

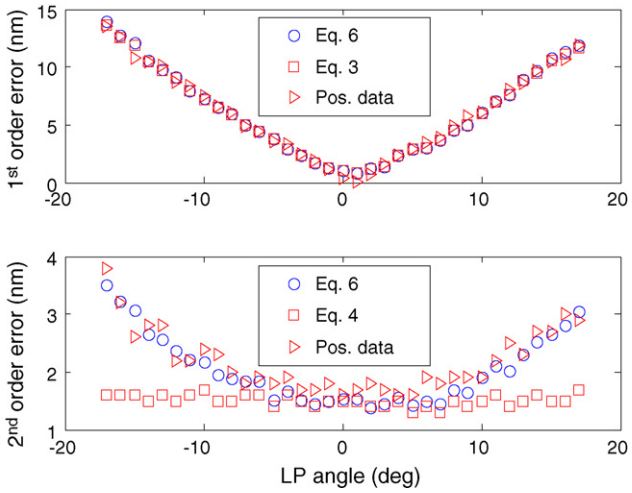

Fig. 23. The magnitudes of first (top) and second (bottom) order periodic errors calculated by Eqs. (3), (4), and (6) are compared to magnitudes computed using the discrete Fourier transform of position data. The agreement is good for first order error, but only Eq. (6) reproduces the second order error.

of the first and second order periodic errors than Eqs. (3) and (4), respectively, which consider only two periodic error components – either γ_0 and γ_1 (first order, Eq. (3)) or γ_0 and γ_2 (second order, Eq. (4)) – especially for significant misalignments from nominal.

Results for a medium misalignment case (5° half wave plate angular misalignment) are provided in Figs. 22 and 23. Trends in γ_0, γ_1, and γ_2 variation similar to those identified in Fig. 19 are observed. This yields the same first and second order periodic error behavior shown in Figs. 20 and 21. Again, Eq. (6) more closely agrees with the position data periodic error magnitudes.

When the half wave plate is oriented at its nominal angle, the axes of the two polarized light frequencies emitted from the laser head are well aligned with the axes of the polarization dependent optics. This naturally leads to significantly reduced frequency leakage. Fig. 24 shows the power level of the three interference terms as a function of the linear polarizer angle. Very little change in the individual power levels is observed and the attenuation between the intended *AC Interference* signal, γ_0, and *AC Reference*, γ_1, and leakage induced *AC Interference*, γ_2, signals is on the order of 33 dBm. Because the signal power levels are constant with the linear polar-

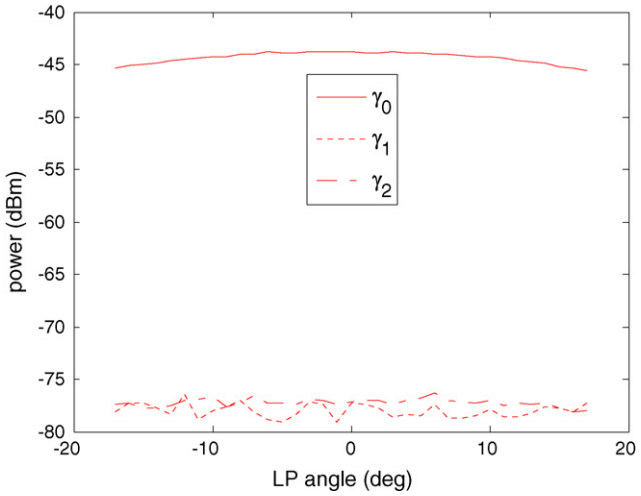

Fig. 24. Variation of γ_0, γ_1, and γ_2 with linear polarizer (LP) angle. The half wave plate was fixed at its nominal orientation (a well aligned configuration). All three signals are nearly constant.

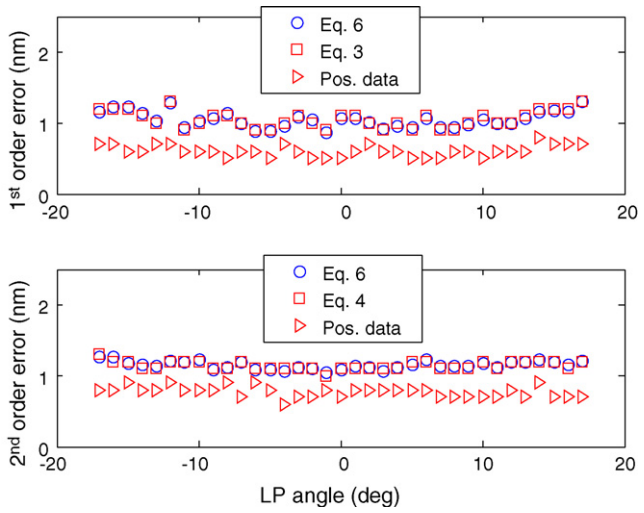

Fig. 25. The magnitudes of first (top) and second (bottom) order error calculated by Eqs. (3), (4), and (6) agree with the position data results because γ_1 and γ_2 do not vary with linear polarizer angle for the well aligned system.

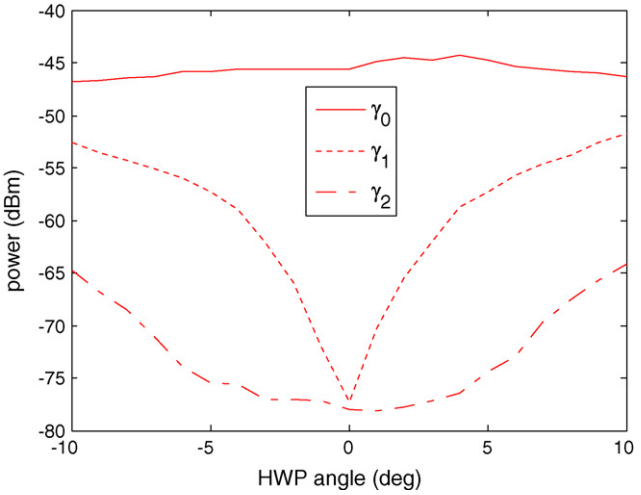

Fig. 26. Variation of γ_0, γ_1, and γ_2 with half wave plate (HWP) angle. The linear polarizer was misaligned by 17° from nominal. Both γ_1 and γ_2 vary.

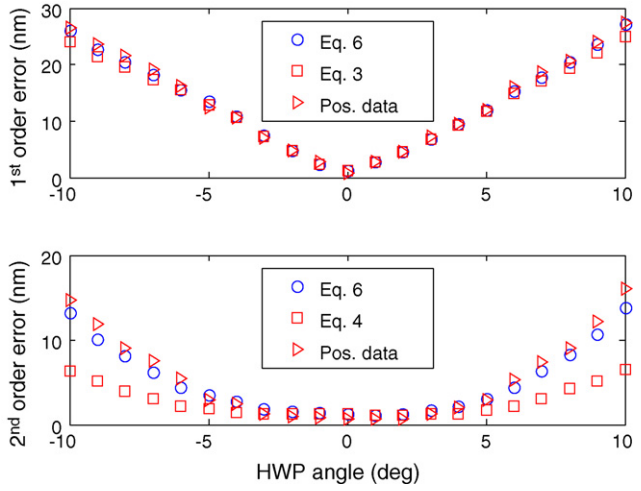

Fig. 27. The magnitudes of first (top) and second (bottom) order error calculated by Eqs. (3), (4), and (6) are compared to position data error magnitudes (the linear polarizer misalignment angle was 17° from nominal). Improved agreement is observed for Eq. (6) results, particularly in the second order error case at large misalignments.

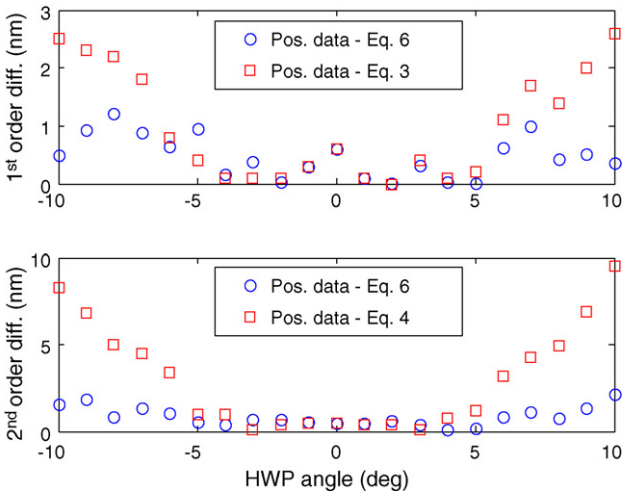

Fig. 28. Differences between magnitudes from Eqs. (3), (4), and (6) calculations and discrete Fourier transform of position data; first order (top) and second order (bottom). The differences were determined from the errors displayed in Fig. 27.

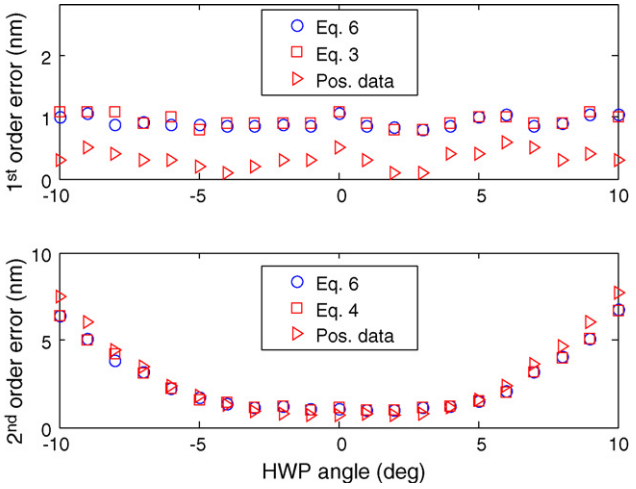

Fig. 30. The magnitudes of first (top) and second (bottom) order error calculated by Eqs. (3), (4) and (6) agree with the position data error magnitudes (the linear polarizer angle was fixed at its nominal orientation). Note that only γ_2 varies, while γ_1 remains constant.

izer angle, the first and second order errors calculated by Eqs. (3), (4) and (6) are also constant and agree with the periodic error magnitudes determined from the position data; see Fig. 25.

We next consider variation of the half wave plate angle. Fig. 26 displays results for a 17° angular misalignment of the linear polarizer. This figure shows that, while both the *AC Reference*, γ_1, and leakage induced *AC Interference*, γ_2, terms vary, γ_1 exhibits higher sensitivity to the half wave plate angle. Fig. 27 displays the corresponding first and second order periodic error comparisons. As seen previously, Eq. (6) results agree more closely with the position data error magnitudes, particularly for second order error under significant misalignments. Fig. 28 shows the associated error magnitude differences.

In Fig. 29, the linear polarizer was set at its nominal orientation and the half wave plate angle was varied. It is seen that only the leakage induced *AC Interference* term, γ_2, varies. The first order error is therefore constant and Eqs. (3) and (6) results agree with the position data first order error magnitudes; see the top panel of Fig. 30. Similarly, both Eq. (4) and (6) results agree with the position data second order error magnitudes as seen in the bottom panel of Fig. 30. Eq. (4) agreement occurs because γ_1 does not change with the half wave plate angle orientation.

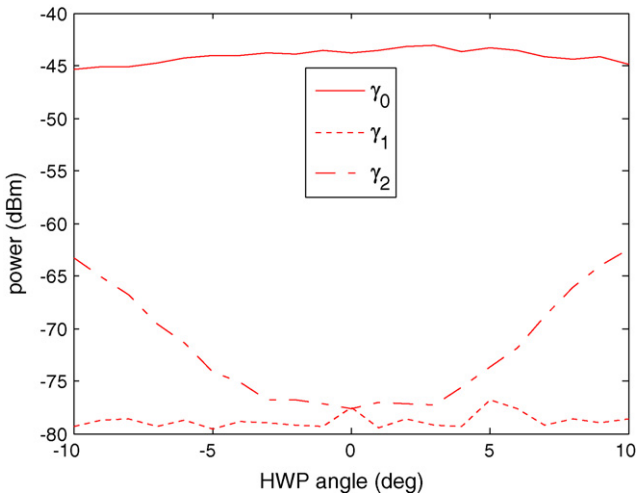

Fig. 29. Variation of γ_0, γ_1, and γ_2 with half wave plate (HWP) angle. The linear polarizer was fixed at its nominal orientation. Only γ_2 varies.

Figs. 31 and 32 show first and second order periodic errors from multiple measurements. The discrete Fourier transform magnitudes of periodic error from position data (phase measuring electronics) is shown in Fig. 31. The spectrum analyzer data, determined from a Monte Carlo evaluation of Eq. (6), is provided in Fig. 32, where the maximum values are again shown. Good agreement is seen for both periodic error orders in all cases.

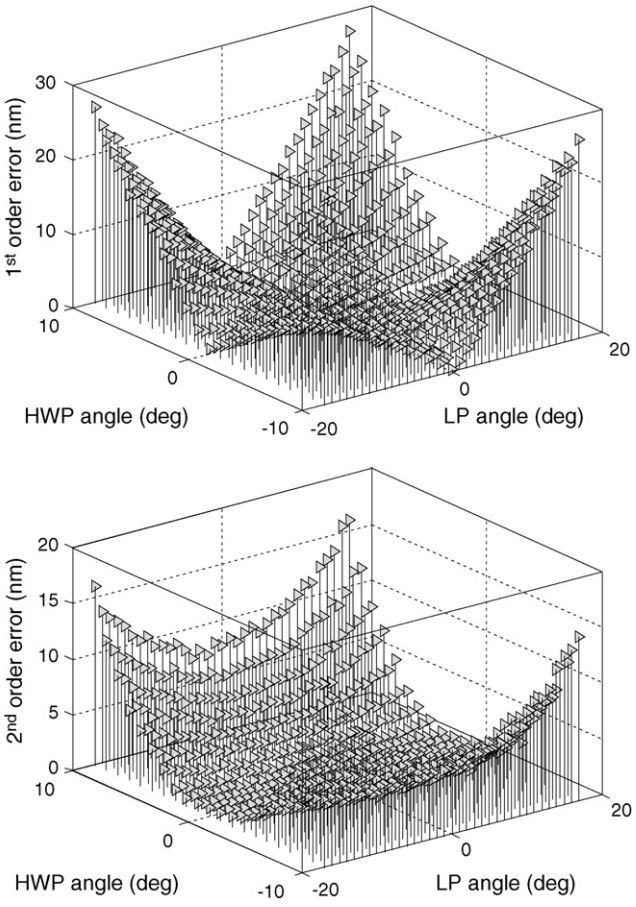

Fig. 31. Periodic errors for half wave plate/linear polarizer parameter study. The errors were obtained from the discrete Fourier transform of position data. First order periodic error is shown in the top panel and second order in the bottom.

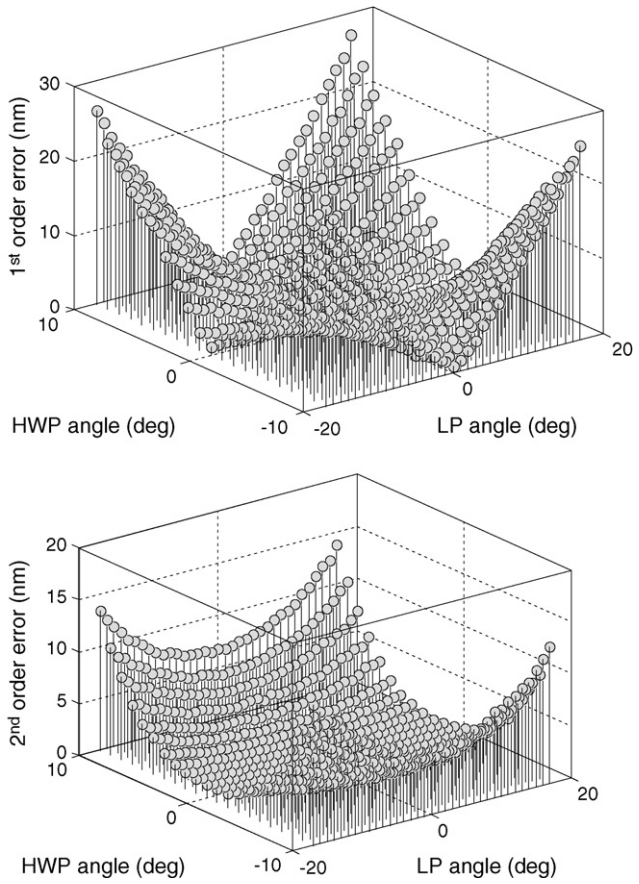

Fig. 32. Periodic errors for half wave plate/linear polarizer parameter study obtained from the spectrum analyzer data and Monte Carlo evaluation of Eq. (6) (the maximum values from the simulation are shown). First order periodic error is displayed in the top panel and second order in the bottom.

As a final example, Fig. 33 shows the discrete Fourier transform of position data collected using a misaligned system (half wave plate angle is 5° from nominal and the linear polarizer is 10° from nominal). The existence of third order error is observed. The magnitudes are: 6.3 nm (first order), 2.1 nm (second order), and 0.3 nm (third order). The power levels of the three interference terms using

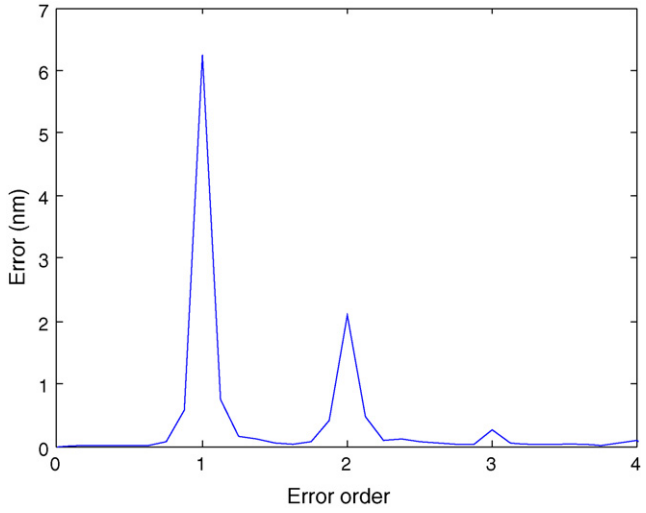

Fig. 33. The spectrum of position data (normalized to error order) contains first, second, and third order periodic error. The data was obtained for 5° half wave plate and 10° linear polarizer misalignments from their nominal angles.

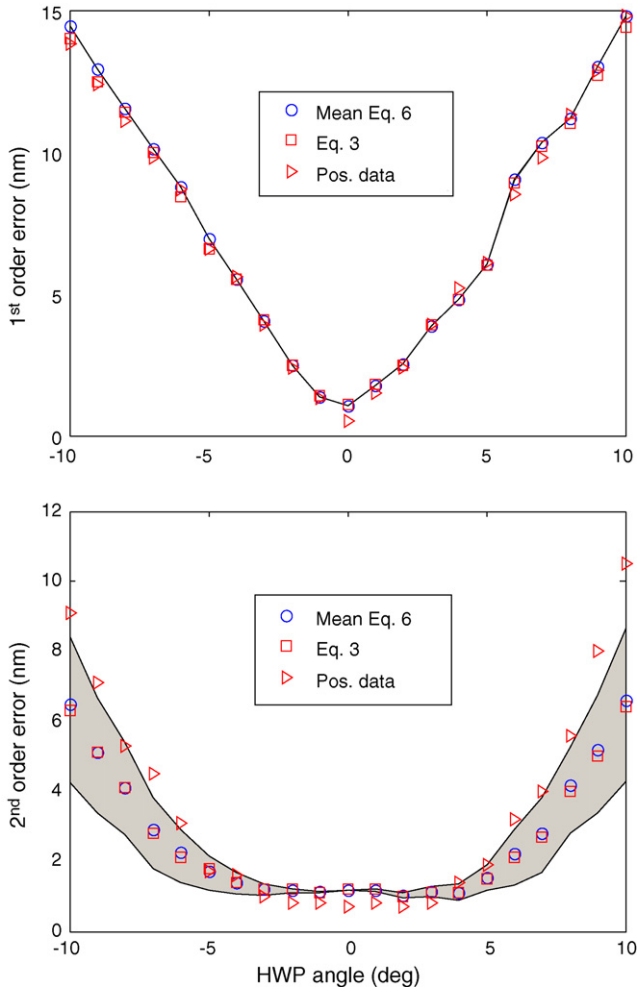

Fig. 34. The magnitudes of first (top) and second (bottom) order periodic errors calculated by Eqs. (3), (4) and (6) are compared to the position data error magnitudes. Eq. (6) Monte Carlo simulation results include the full distribution of values (indicated by the gray band).

the same configuration were also measured using the spectrum analyzer; the values were: $\gamma_0 = -45.5$ dBm, $\gamma_1 = -62.8$ dBm, and $\gamma_2 = -74.5$ dBm. The corresponding maximum error magnitudes calculated using a Monte Carlo evaluation of Eq. (6) are: 6.1 nm (first order), 2.0 nm (second order), and 0.2 nm (third order). These results correspond closely with the position data magnitudes.

7. Discussion

The data shown in Fig. 34 were collected with a 10° linear polarizer misalignment, while the half wave plate angle was varied. Maximum, minimum, and mean values of the first and second order error magnitudes determined from a Monte Carlo evaluation of Eq. (6) are presented, together with Eq. (3) and (4) results and position data magnitudes. It is seen that the spread in first order error values obtained from Eq. (6) (top panel of Fig. 34) is small. This suggests that the calculation is not particularly sensitive to the initial phases of the three interference terms. For the second order error calculations (bottom), however, the spread is significant. As reported in the previous figures, the maximum errors (the upper bound of the band) from simulation agree well with the position data error magnitudes. The mean values, however, track more closely with Eq. (4) results. This outcome is counterintuitive and suggests that our assumption of uncorrelated arbitrary phases may be incorrect. This can be investigated further in future studies. However, in a practi-

cal sense, Eq. (6) still provides accurate estimates for both first and second periodic error magnitudes (under arbitrary misalignments) provided the maximum value from the Monte Carlo evaluation is applied.

8. Conclusions

This paper detailed the Monte Carlo evaluation of a single equation that may be used to determine periodic error magnitudes from spectrum analyzer data. The required magnitudes of the individual periodic error contributors were obtained by recording the optical interference signal during constant velocity target motion using a spectrum analyzer. In the new approach, the general case was treated, where both first and second order error components exist and arbitrary initial phase values are considered. Experiments showed good agreement between the new approach and periodic error magnitudes determined from the discrete Fourier transform of position signals collected using traditional phase measuring electronics, provided the maximum value from the Monte Carlo evaluation of the equation was used.

Acknowledgements

This work was supported by the National Science Foundation (DMI-0555645) and Agilent Technologies, Inc. Any opinions, findings, and conclusions or recommendations expressed in this material are those of the authors and do not necessarily reflect the views of these agencies. The authors would also like to thank V. Badami and J. Beckwith for helpful discussions during the completion of this work.

References

[1] Patterson S, Beckwith J. Reduction of systematic errors in heterodyne interferometric displacement measurement. In: Proceedings of the 8th International Precision Engineering Seminar (IPES). 1995. p. 101–4.
[2] Badami V, Patterson S. A frequency domain method for the measurement of nonlinearity in heterodyne interferometry. Precision Engineering 2000;24(1):41–9.
[3] Schmitz T, Beckwith J. An investigation of two unexplored periodic error sources in differential-path interferometry. Precision Engineering 2002;27(3):311–22.